X International Conference on Computational Methods for Coupled Problems in Science and Engineering
COUPLED PROBLEMS 2023
M. Papadrakakis, B. Schrefler and E. Oñate (Eds)

DEVELOPMENT OF AN FSI ENVIRONMENT FOR THE AERODYNAMIC PERFORMANCE ASSESSMENT OF FLAPPING WINGS

R. POLETTI[*†], M. BARUCCA[*§], L. KOLOSZAR[*], M. A. MENDEZ[*] AND J. DEGROOTE[†]

[*]Environmental and Applied Fluid Dynamics Department
von Karman Institute for Fluid Dynamics
Waterloosesteenweg 72, B-1640 Sint-Genesius-Rode, Belgium
e-mail: romain.poletti@vki.ac.be

[§]Department of Mathematics
Politecnico di Milano
Piazza Leonardo da Vinci 32, 20133 Milano, Italy

[†]Department of Electromechanical, Systems and Metal Engineering, Faculty of Engineering and Architecture
Ghent University
Sint-Pietersnieuwstraat 41, 9000 Gent, Belgium
e-mail: Joris.Degroote@UGent.be

Key words: Flapping drones, Flexible wing aerodynamics, Fluid-structure interaction, Dynamic mesh, Deformable overset method

Abstract. Insects and birds take advantage of their flexible wings to modulate the aerodynamic forces and increase their flight efficiency. A deep understanding of the aeroelastic benefits could be valuable to design Flapping Wing Micro Air Vehicles (FWMAVs) that exploit nature's full potential. This work presents an open-source, high-fidelity, Fluid-Structure Interaction solver (FSI) to simulate flapping and deforming wings. The proposed approach uses the code CoCoNuT to couple the Computational Structural Mechanics (CSM) software Kratos Multiphysics with the Computational Fluid Dynamics (CFD) software OpenFOAM. The coupling code relies on the Interface Quasi-Newton with Inverse Jacobian method (IQNI). The CSM evaluates the wing deformation using a classic Finite Element Method with shell elements, while the CFD solver uses the deformable overset method. In the CFD solver, the deformation of the wing is interpolated onto the grid's boundaries to accurately simulate wings with large motion and deformation. The FSI solver is tested in the case of an airfoil in heave motion and validated with experimental data. The results demonstrate the strong influence of wing deformation on its aerodynamic performance.

1 INTRODUCTION

Insects and birds reach unmatched aerodynamic performance in various flight conditions. Hummingbirds are the smallest vertebrates to perform hovering and extreme aerobatic manoeuvres [1]; mosquitoes can lay eggs while stably flying in disturbed conditions [2]; owls fly

silently to stealthy catch prey [3], etc. Flapping Wing Micro Air Vehicles (FWMAVs) attempt to mimic these species, but a deep understanding of their flight physics is still missing. An open question is the role of wing flexibility in achieving such aerodynamic performance, whether in the case of a membrane wing, as in the case of a bat, or a feathered wing, as in the case of a bird.

Wind tunnel experiments can be used to study flapping aerodynamics but usually focus on specific conditions in terms of shape, flexibility, and motion. Fluid-structure interaction simulations offer a more versatile alternative. These allow to analyze and optimize different wing shapes, kinematics, and materials with reduced set-up efforts. Recently, [4] studied the influence of the flapping frequency for insect-scale wings while [5] optimized the twist level of rectangular wings and [6] analyzed the influence of wing flexibility on bat wings. These studies couple Computational Structural Mechanics (CSM) and Computational Fluid Mechanics (CFD) solvers through a coupling code. The FSI frameworks usually compromise accuracy or generality in implementing the solvers or their coupling. For example, the CFD is often carried out with the immersed boundary method, which can fail to accurately capture the smallest structures formed near the wing surface.

The present work proposes a high-fidelity and open-source fluid-structure environment that can accurately simulate wings undergoing large flapping motions and large deformations. The selected test case is a 2D heaving and deforming airfoil, described in Section 2. The CSM, the CFD and their coupling are described in section 3. Section 4 validates the simulations against experimental data. The analysis of vorticity and Finite Time Lyapunov Exponents (FTLE) fields reveals the influence of wing flexibility on thrust, lift and propulsive efficiency.

2 MODEL DEFINITION

The FSI environment is tested for a flexible wing in heave motion, for which an experimental characterization was presented in [7]. The experiments were carried out in a water tunnel at constant horizontal uniform flow U_∞. The selected wing profile is illustrated in Figure 1 and is made of two parts: (1) a rigid teardrop airfoil and (2) a thin flexible plate made of steel. The airfoil occupies one-third of the total chord, and Table 1 lists the main physical parameters of the problem. The heave motion is introduced with a harmonic vertical displacement with amplitude A and frequency f. This is defined at the leading edge by $y_{LE} = A\cos(2\pi f t)$. The plate follows y_{LE} but also deforms along its chord depending on the steel density ρ_s, elasticity modulus E, Poisson ratio γ and plate thickness b (Table 1). Two dimensionless parameters characterize the flow: the Reynolds number $\mathrm{Re} = U_\infty c/\nu_f = 9000$ and the Strouhal number $\mathrm{Sr}=2fA/U_\infty = 0.34$, which defines the ratio between the heaving and incoming velocity. The bending stiffness coefficient $\lambda = Eb^3/(6\rho_s U_\infty^2 c^3) = 0.08$ characterizes the deformation of the plate for the conditions of Table 1 but different values of the thickness b are also investigated. The experimental work [7] provides numerous validation data such as the instantaneous position of the plate trailing edge $y_{TE}(t)$ and the aerodynamic force coefficients:

$$C_T = \frac{F_x}{0.5\rho U_\infty^2 c} \qquad (1) \qquad\qquad C_L = \frac{F_y}{0.5\rho U_\infty^2 c} \qquad (2)$$

If positive, F_x defines the thrust force and F_y the lift. The propulsive efficiency quantifies the balance between the achieved thrust and its energy cost. This can be defined as

$$\eta = \frac{\overline{TU_\infty}}{\overline{F_y \dot{y}_{LE}}}\,, \tag{3}$$

where TU_∞ is the power extracted by the wing while $F_y \dot{y}_{LE}$ is the input power required to flap. The overbar in both terms denotes averaging over one cycle.

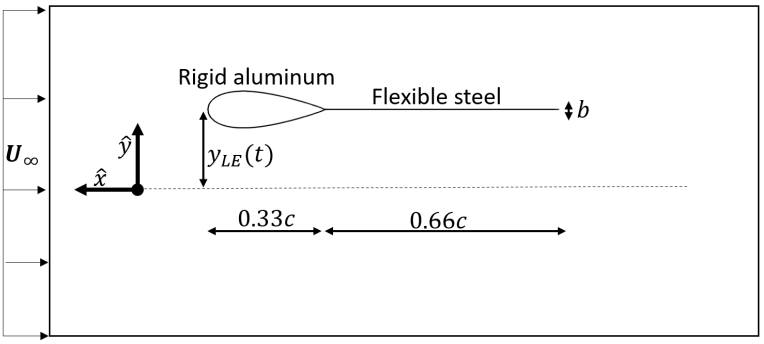

Figure 1: Schematic of the water tunnel and the wing formed of a rigid airfoil and a flexible plate

Symbol	Value	Unit
U_∞	0.1	m/s
c	0.09	m
A	0.0175	m
f	0.96	Hz
b	5.04e-5	m
ρ_s	7850	kg/m^3
E	2.05e11	N/m^2
γ	0.3	–

Table 1: Main parameters of the heaving airfoil [7]

3 METHODS

The wing heaving generates aerodynamic forces on its surface due to its surrounding flow. The loads deform the flexible plate which subsequently alters the fluid forces. The CFD software for the flow equations is described in section 3.1 while the CSM software for the plate deformation is described in section 3.2. The fluid-structure interface to couple loads and deformations at the flexible plate is described in section 3.3.

3.1 The CFD model

The present section describes the development of a high-fidelity CFD environment to simulate the flow dynamics around moving and deforming wings in the open-source software OpenFOAM v2012. The finite volume code discretizes the unsteady and incompressible Navier-Stokes equations. The selected solver implements the PIMPLE algorithm for pressure-velocity coupling and the overset method to adapt the grid according to the wing's motion. The overset method, also called chimera technique [8], re-formulates the momentum equations with the Arbitrary-Lagrange-Euler (ALE) method:

$$\frac{\partial \boldsymbol{U}}{\partial t} + \boldsymbol{U} \cdot \boldsymbol{\nabla}(\boldsymbol{U} - \boldsymbol{U_g}) = -h\boldsymbol{\nabla p} + \nu \boldsymbol{\Delta U}\,, \tag{4}$$

where $\boldsymbol{U}$ is the flow velocity, p is the kinematic pressure, h is a cell's role indicator discussed hereafter and $\boldsymbol{U_g}$ is the grid velocity of the two overlapping grids that form the computational domain (see Figure 2.A). A small component grid follows the wing ($\boldsymbol{U_g} = (0, \dot{y})$) and overlaps a larger, static, background grid ($\boldsymbol{U_g} = (0, 0)$). The flow equations are solved simultaneously on both grids. These exchange pressure and velocity fields through interpolation (strong coupling

[9]). Figure 2.B summarises the inter-grid communication. Blue "activated" cells solve the flow equations (equation 4). Red "holes" are inactive cells of the background that overlap with the wing. The indicator function h acts as a mask to zero the velocity on inactive cells and ensures that these do not affect active cells (equation 4). Green cells are interpolated cells that receive information from neighbour cells of the other grid, using a weighted average of the form:

$$\boldsymbol{U_{int}} = \sum_{j \sim \text{donors}} \boldsymbol{U_j} \omega_j \,, \tag{5}$$

with U_j the velocity at the j-th donor cell and ω_j define the interpolation weights based on the inverse distance scheme. Equation 5 completes then the boundary conditions on the component grid interface and hole boundary (Figure 2.B). The reader is referred to [9] for more details on the overset method.

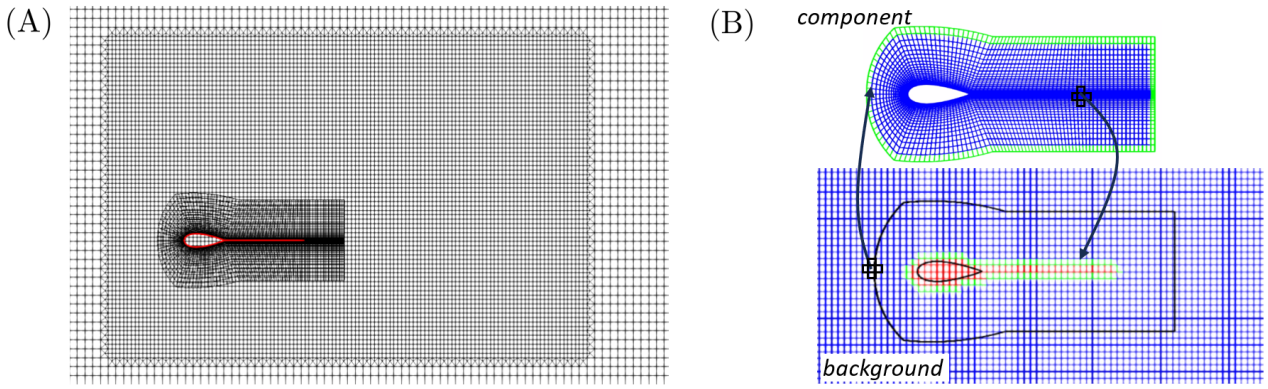

Figure 2: (A) Overset grid composed of a component grid fitted around the wing and overlapped on a background cartesian grid. (B) Illustration of the working principle of the overset method. Blue: solved cells, Red: inactive cells, Green: interpolated cells. Interpolation occurs from certain solved cells (donors) to the interpolated cells

Figure 2.A shows a grid made of $23k$ hexahedral cells. The component grid defines a C-grid topology of one chord width, taken normally to the profile [10]. A zero cell-thickness baffle simplifies the wing's plate taking advantage of its small thickness compared to its chord dimension (Table 1). The background grid is 10 chords long which prevents boundary influence on the wing. The background grid contains a refinement zone along the wing trajectory such that the cell size of the background and component grid coincides at their interface. This minimizes inter-grid interpolation errors as shown in previous works [9, 11].

In the classic overset implementation, the component grid conserves its cell size and therefore can only follow rigid motions of the wing. A deforming mesh technique must complement the overset method to morph the component grid cells according to the plate state. This leads to the deformable overset method, with mesh deformation carried out via spring analogy, pseudo-solid method or the Laplace smoothing equation [12]. The latter is computationally cheaper and gave accurate aerodynamic predictions on similar cases [13]. It distributes non-uniformly the mesh deformation by solving:

$$\boldsymbol{\nabla} \cdot (\Gamma \boldsymbol{\nabla}(\boldsymbol{p_d})) = 0 \,, \tag{6}$$

where $\mathbf{p_d}$ is the field of point displacement updating the point coordinates of the component grid cells $\mathbf{p_{k+1}} = \mathbf{p_k} + \mathbf{p_d}$ for each time step k while Γ is the diffusivity that drives how the mesh motion spreads. This parameter is inversely proportional to the distance from the wing to strongly deform cells far from the wing and preserve mesh quality close to the wing [14]. Equation (6) is solved with $\boldsymbol{p_d} = (0, y_{LE})$ on the airfoil surface, $\boldsymbol{p_d}$ imposed by the structural mechanics' solver on the plate surface, and typically also with Neumann conditions ($\nabla \boldsymbol{p_d} = 0$) on the external boundaries. This common condition propagates the mesh deformation from the body towards the boundary (region 1 in Figure 3.A). However, for region 2, no moving parts are present so the Neumann condition forces the cells to remain mostly static. This rapidly brings negative volume cells at the interface between region 1 and 2 (Figure 3.A).

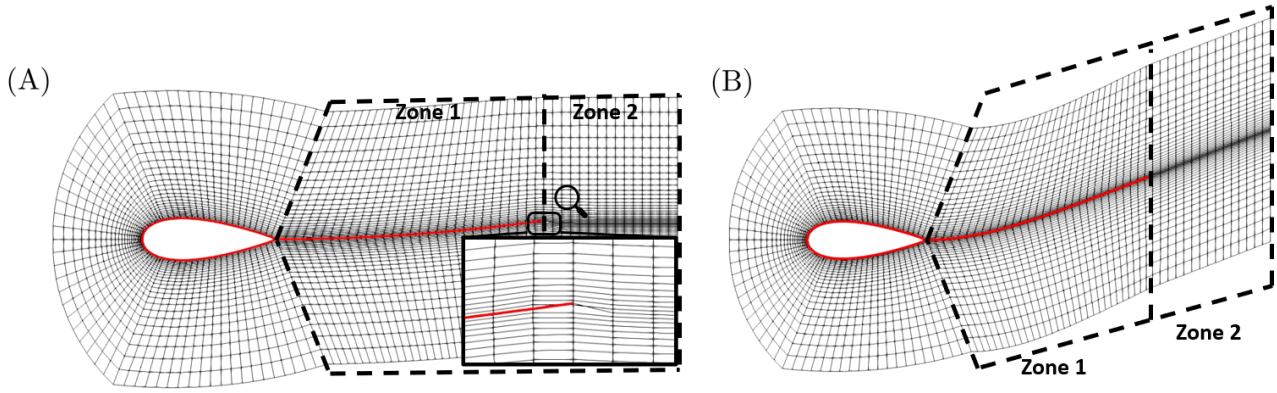

Figure 3: Deformed component grid with zero gradient conditions (A) and interpolation conditions (B) on the external boundaries

The implemented solution replaces the Neumann condition with a custom expression. It enforces a deformation similar to the wing at the component grid boundary by extrapolating the known state of the wing. Component boundaries of zone 1 implement a one-to-one interpolation, which takes advantage of the grid topology to directly impose the point displacements of the wing on the boundary cells $\boldsymbol{p_d} = \boldsymbol{p_{d,wing}}$. For region 2, a line is fitted from the last two cell vertices of the plate. The component patch of region 2 uses this linear expression to compute its y-coordinates while the x-coordinates are the x displacements measured at the plate's tip. As shown in Figure 3.B, the implemented method preserves high-quality cells even in case of large deformations of the wing.

The momentum equation (4) is solved without turbulence modeling, given the moderate Reynolds number. This choice was validated against Large Eddy Simulation (LES) for 3D rigid wings in [11]. Concerning numerical schemes, second-order, central Gauss schemes with limiters discretize the spatial terms. A backward second-order implicit scheme discretizes the time derivative term with fixed time steps ($\Delta t \sim 1/(1000 f)$).

3.2 The CSM model

The structural mechanics' solver maps the fluid loads to a deformation field $\boldsymbol{p_d}$ on the plate thanks to the momentum conservation:

$$\rho_s \frac{\partial^2 \boldsymbol{p_d}}{\partial t^2} - \boldsymbol{\nabla \cdot \tau_s} = \boldsymbol{f_s}\,, \tag{7}$$

where $\boldsymbol{\tau_s}$ is the stress tensor of steel that connects to the strains with the linear elasticity theory and $\boldsymbol{f_s}$ is the body force. The software is Kratos Multiphysics which is open-source, multi-physics, and based on the finite element method. An in-house code also converts the OpenFOAM grid of the plate into a Kratos-compatible format. The grid defines 30 corotational, 4 nodes, 6 degrees of freedom shell elements. Shell elements save computation time by replacing 2D xy elements with a 1D element at the center line. This assumes a small thickness compared to the chord dimension ($t/c << 10$). Equation (7) is then solved for all the nodes of the plates except for the LE which moves according to the heave motion. The time scheme is the implicit Bossak and uses the same time steps as the CFD computation.

3.3 The coupling algorithm

Figure 4 illustrates the architecture of the FSI environment coupling CFD and CSM computations. This partitioned approach allows reusing dedicated software (OpenFOAM and Kratos Multiphysics) that use optimal methods to solve flow and structure problems but requires a coupling unit to satisfy equilibrium conditions at the FSI interface [15]. The open-source code CoCoNUT takes care of the coupling thanks to three main packages, herein briefly described.

1. *A coupling solver* to ensure that the deformation field $\boldsymbol{p_d}$ is the same in the CFD and the CSM. This is ensured by running both solvers multiple times. At each time step k, starting from an initial guess $\boldsymbol{p_d}^{(n)}$ with $n = 0$, the coupling solver runs a CFD simulation to compute the pressure p and shear stress $\boldsymbol{\tau}$, and then runs a CSM simulation with these to compute an update $\boldsymbol{p_d}^{(n+1)}$. This is repeated until the residual $\boldsymbol{p_d}^{(n+1)} - \boldsymbol{p_d}^{(n)}$ falls below a tolerance. The residual minimization is carried out using the Interface Quasi-Newton with Inverse Jacobian method (IQNI) [15]. The IQNI estimates the unknown inverse Jacobian thanks to previous solver iterations' input and output pairs. The reader is referred to [16] for more details on the IQNI method and other convergence techniques. The method ensures a stable and fast convergence for strongly coupled problems with a high added-mass effect.

2. *Two solver wrappers*, controlling the computations in the CFD and CSM solver and the communication between them. It reports when a computation must be performed and when the results must be transmitted/received at the FSI interface.

3. *A solver mapper*, to interpolate the loads from the fluid grid to the structural grid and vice-versa. In this work, interpolation is not needed since the flow and structure solver grids coincide.

4 RESULTS

4.1 Code validation

This section validates the FSI environment developed in section 3 for the setup defined in table 1. The wing first heaves down from $t/T = 0$ to $t/T = 0.5$ (downstroke) and moves

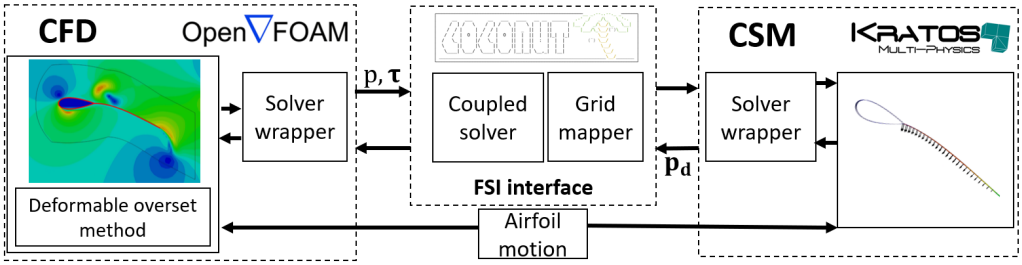

Figure 4: Block diagram of the FSI environment defined with OpenFOAM (CFD), Kratos Multiphysics (CSM) and CoCoNut

back up afterwards (upstroke). Figure 5 compares the TE displacement from the CoCoNut environment with the original experiments performed by Heathcote *et al* [7] and the numerical simulations by Kang *et al*, who used different CFD and CSM codes [17]. The numerical results closely match the experimental data. The minor discrepancies could be attributed to experimental uncertainties or hysteresis since different maximum displacements of the trailing edge are reported in [7] during the downstroke and upstroke ($|y_{TE}(t \approx 0.15T)| < |y_{TE}(t \approx 0.65T)|$). Comparing the numerical results, the TE displacements coincide almost perfectly. Nevertheless, the literature results were slightly offset to be in phase with the experiments.

Figure 6 shows the pitch phase angle (PPA) to illustrate that the FSI environment was also validated for different flexibility (thickness to chord ratios b/c) and Strouhal numbers. The pitch phase angle is the phase difference between the tangent of the pitch angle $(y_{LE} - y_{TE})/c$ and the leading edge position y_{LE}. The numerical results capture the same trend as the experiments: the PPA decreases when the flexibility or the Strouhal number increases [7].

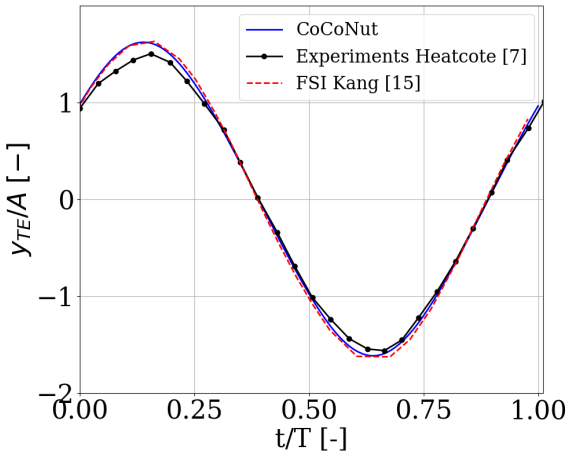

Figure 5: Comparison of TE displacement of the plate during one flapping cycle with literature data [7][17]

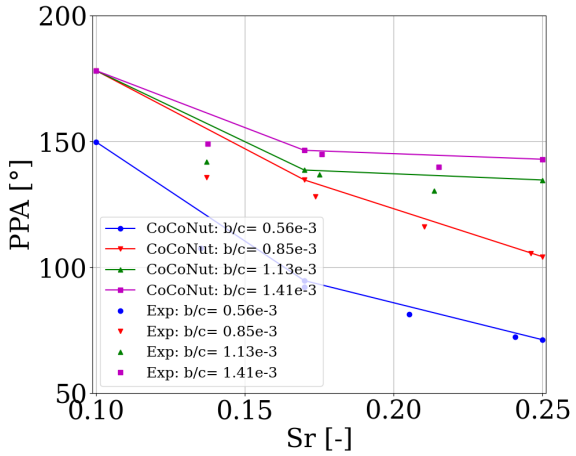

Figure 6: Comparison of the pitch phase amplitude (PPA) for different Strouhal numbers Sr and flexibilities with literature data [7]

The most flexible plate requires $\sim$ 2.5 h on two cores to complete one cycle. The CFD computation takes 85% of this time, the structural mechanics 11% and the coupling code solely 4%. On average, the IQNI necessitates six coupling iterations to achieve convergence at each time step. These numbers represent the worst-case scenario as the computational cost decreases when the plate stiffens.

4.2 Aerodynamics analysis

This last section demonstrates the FSI environment's ability to reveal the influence of wing flexibility on its aerodynamics. Figure 7.A shows that flexibility increases the maximum amplitude of the TE displacement and also changes the TE phase with respect to the LE motion (which coincides with the TE displacement of the stiff plate). This results from the fluid inertia [7], which also increases thrust (Figure 7.B). The thrust is positive regardless of the flexibility (along $+\hat{x}$ in Figure 1) as a reverse vortex street forms in the wake for $Sr > 0.17$ [7]. The clockwise and anti-clockwise vortices create a jet that produces a momentum surplus to the freestream flow. Figure 8 and 9 prove this with the out-of-plane vorticity field. Coherent structures are also revealed using the contour of the negative Finite Time Lyapunov Exponent (FTLE) field [18]. The wake of the most flexible plate produces stronger vortices, more spaced along $\hat{y}$, generating a stronger and wider jet [7]. An additional reason for increased thrust is merely geometrical: as the deformation increases, the normal vectors become more aligned along the freestream direction, and with them, the aerodynamic loads.

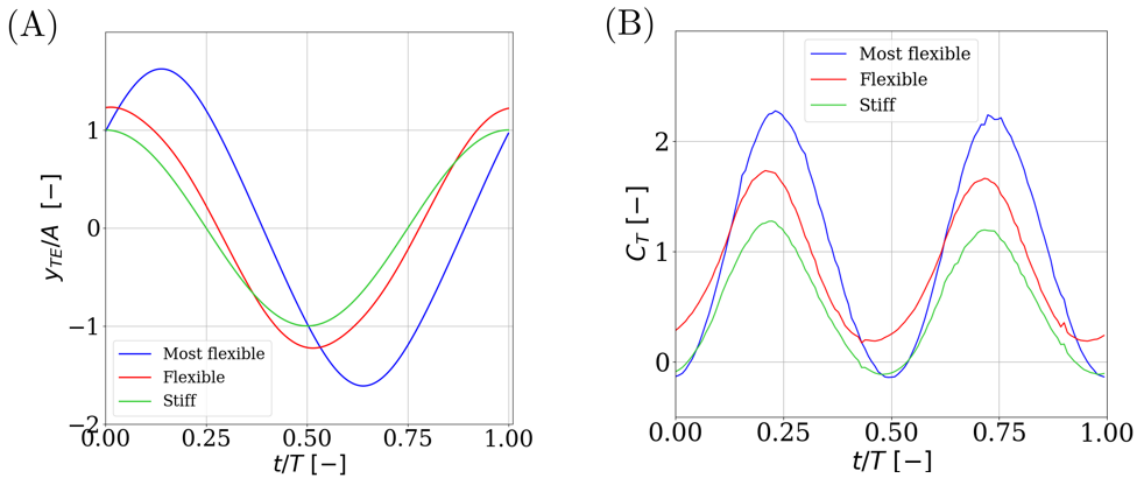

Figure 7: Influence of the plate flexibility on the TE displacement (A) and thrust coefficient C_T (B) during one flapping cycle. Most flexible: $b/c = 0.56e-3$, flexible: $b/c = 1.1e-3$, stiff: $b/c = 4.23e-3$

The plate flexibility also affects the lift production due to the change of the effective angle of attack $\alpha_{eff} = tan^{-1}\frac{-\dot{y}_{LE}}{U_\infty} - tan^{-1}\frac{y_{LE}-y_{TE}}{c}$. The first term defines the relative orientation of the flow with respect to the heaving wing, while the second term is the geometric angle of attack. When the plate bends, the second contribution tends to cancel the first one and hence reduces the lift production (Figure 10).

Finally, it is also interesting to look at the power balance between the thrust and the lift, i.e. the propulsive efficiency (equation (3)).

	Most flexible	Flexible	Stiff
η	0.30	0.21	0.17

Table 2: Influence of the plate flexibility on the propulsive efficiency (equation (3))

For the conditions set by Table 1, increasing flexibility steadily increases efficiency. Figure

8 and 9 display this thanks to the life cycle of the vortical structures generated by a stiff and flexible wing, taking inspiration from similar analyses in [19]. The plate starts at the downstroke ($t/T = 2$), goes down until $t/T = 2.5$, and ends the upstroke at $t/T = 3$.

At the end of each stroke ($t/T = 2$ and $t/T = 2.5$), a Leading Edge Vortex (LEV) forms on the leeward side of the wing (anti-clockwise at the end of the upstroke, clockwise at the end of the downstroke). This LEV is rapidly joined by a second, smaller and counter-rotating vortex at the beginning of the next stroke (LEV2). This vortex pair (LEV=LEV1+LEV2) is well visible on the windward side of the wing where the FTLE contours shape a "mushroom" ($t/T = 2.25$ and $t/T = 2.75$).

In the case of the stiff plate, LEV2 grows as the LEV remains attached to the airfoil. When the airfoil slows down and reverses stroke ($t/T = 2.5$ and $t/T = 2$), the attached LEV sheds at the same time at which a new LEV1 forms on the opposite side of the wing. During the following stroke, a vortex filament links the plate to the vortex while it sheds and rotates along its center (LEV1 taking the place of LEV2 and vice versa). Starting from the end of the cycle ($t/T = 2$ and $t/T = 2.5$), the LEV interacts with the wake vortices. LEV2 merges with the Trailing Edge Vortex (TEV) shed at the end of the previous stroke that rotates in the same direction ($t/T = 2.25$ and $t/T = 2.75$). LEV1 interacts with the attached TEV from the current stroke but without merging despite the same direction of rotation. LEV1 remains a separate coherent structure that bridges the current and previous TEV of the plate ($t/T = 2.5$ and $t/T = 3$).

The dynamics of LEVs and TEVs change significantly with plate flexibility. LEVs are smaller and slide along the plate following its deformation. This allow them to stay attached for almost one complete cycle compared to a half-cycle for the stiff wing. The LEV moves directly from the plate to the wake at the end of each cycle.

The flexible plate also creates stronger TEVs and delays the detachment time slightly after stroke reversal. The shed LEV1 meets then a counter-rotating TEV at the end of each cycle resulting in destructive interference that weakens the LEV and TEV in the wake. For the tested flexibility, this effect is always compensated by the initially stronger TEV (thrust still increases with flexibility). Nevertheless, if the flexibility was further increased, the mean thrust might reach a maximum and then decrease.

The LEV also adversely affects the pressure distribution on the airfoil in terms of efficiency (equation 3) according to the superior lift that a strong LEV generates. It is then preferable to have a lower effective angle of attack that goes with higher flexibility. Nevertheless, overly large flexibility weakens the vortex system and penalizes the thrust [7].

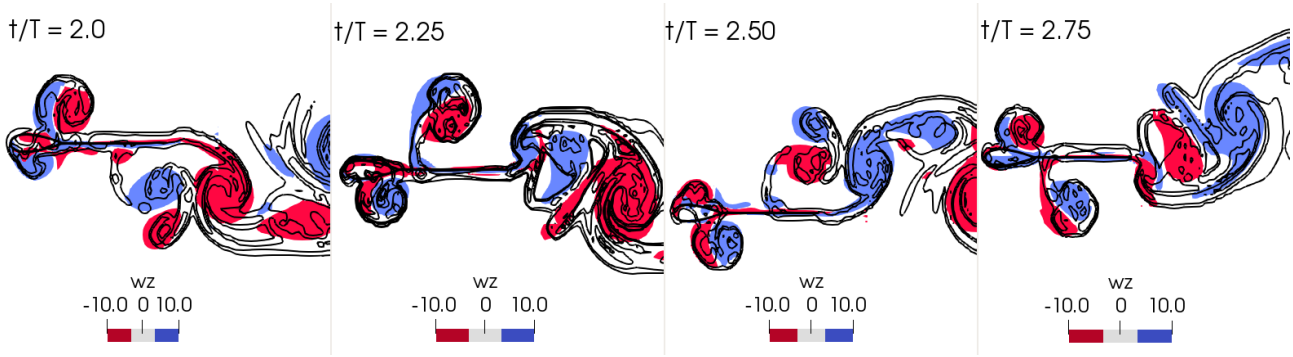

Figure 8: Vorticity field and contour of the FTLE for a complete cycle of the stiff plate. Blue: counter-clockwise vortices, red: clockwise vortices

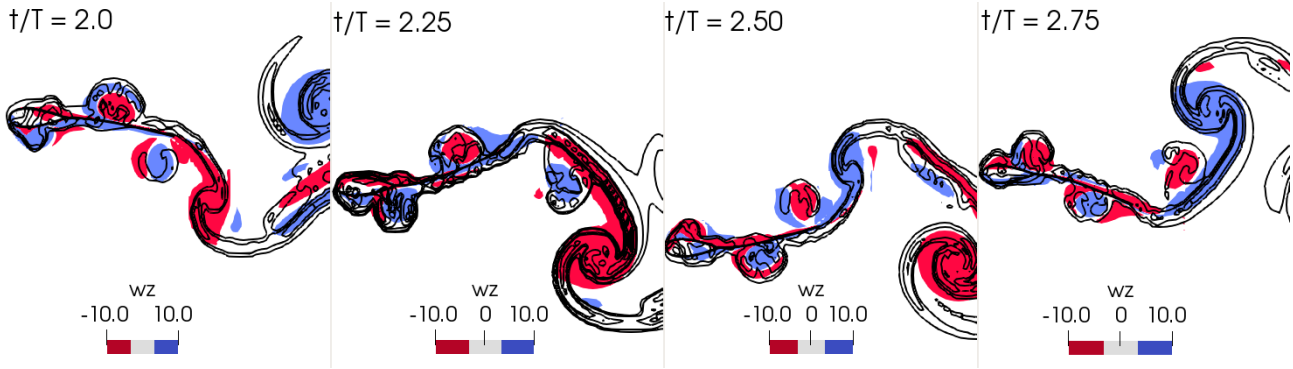

Figure 9: Vorticity field and contour of the FTLE for a complete cycle of the most flexible plate. Blue: counter-clockwise vortices, red: clockwise vortices

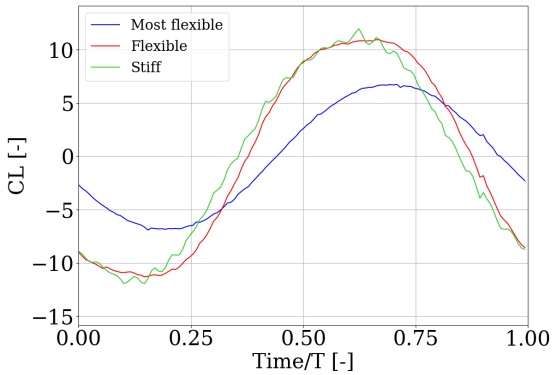

Figure 10: Influence of the plate flexibility on the lift C_L during one flapping cycle. Most flexible: $b/c = 0.56e-3$, flexible: $b/c = 1.1e-3$, stiff: $b/c = 4.23e-3$

5 CONCLUSIONS

This paper presented a fluid-structure interaction environment to simulate flapping and flexible wings. The environment combines three high-fidelity open-source codes (OpenFOAM,

Kratos Multiphysics and CoCoNuT) to simulate the complex aero elasticity of flapping wings. The fluid solver relies on the deformable overset method combining the overset method with a deforming mesh technique. While the method usually distorts cells near the tip of the wing, this work uses an interpolation boundary condition for propagating grid deformation more uniformly. The structure solver relies on the finite element method with shell elements. Finally, the IQNI coupling method prevents numerical instabilities that could arise due to the high added mass. The validation against experimental and numerical data proved that the proposed FSI environment is accurate in heave motion. Aerodynamic analyses have confirmed that wing flexibility generates a peculiar vortical system in the wake, increasing thrust and propulsive efficiency. The environment will be extended to 3D semi-elliptical wings in future works, taking advantage of the similarities with the presented 2D case.

REFERENCES

[1] Diana D Chin and David Lentink. Flapping wing aerodynamics: from insects to vertebrates. *Journal of Experimental Biology*, 219(7):920–932, 2016.

[2] Richard J Bomphrey, Toshiyuki Nakata, Nathan Phillips, and Simon M Walker. Smart wing rotation and trailing-edge vortices enable high frequency mosquito flight. *Nature*, 544(7648):92–95, 2017.

[3] Nikolaos Beratlis, Francesco Capuano, Krishnamoorthy Krishnan, Roi Gurka, Kyle Squires, and Elias Balaras. Direct numerical simulations of a great horn owl in flapping flight. *Integrative and Comparative Biology*, 60(5):1091–1108, 2020.

[4] Yueyang Guo, Wenqing Yang, Yuanbo Dong, and Jianlin Xuan. Numerical investigation of an insect-scale flexible wing with a small amplitude flapping kinematics. *Physics of Fluids*, 34(8):081903, 2022.

[5] Qi Wang, JFL Goosen, and F Van Keulen. An efficient fluid–structure interaction model for optimizing twistable flapping wings. *Journal of Fluids and Structures*, 73:82–99, 2017.

[6] Sushrut Kumar, Jung-Hee Seo, Dimitri Skandalis, Cynthia Moss, and Rajat Mittal. Fluid-structure interaction of bat-inspired membrane wings. *Bulletin of the American Physical Society*, 2022.

[7] Sam Heathcote and Ismet Gursul. Flexible flapping airfoil propulsion at low reynolds numbers. *AIAA Journal*, 45(5):1066–1079, 2007.

[8] Joseph L Steger, F Carroll Dougherty, and John A Benek. A chimera grid scheme. 1983.

[9] Hidajet Hadzic. *Development and application of finite volume method for the computation of flows around moving bodies on unstructured, overlapping grids*. Technische Universität Hamburg, 2006.

[10] Camli Badrya, Ananth Sridharan, James D Baeder, and Christopher M Kroninger. Multi-fidelity coupled trim analysis of a flapping-wing micro air vehicle flight. *Journal of Aircraft*, 54(5):1614–1630, 2017.

[11] Andre Calado, Romain Poletti, Lilla Koloszar, and Miguel A. Mendez. A robust data-driven model for flapping aerodynamics under different hovering kinematics. *Physics of Fluid*, Currently in revision.

[12] Tianhang Xiao, Ning Qin, Dongming Luo, and Shuanghou Deng. Deformable overset grid for multibody unsteady flow simulation. *AIAA Journal*, 54(8):2392–2406, 2016.

[13] Michael Alletto. Comparison of overset mesh with morphing mesh: Flow over a forced oscillating and freely oscillating 2d cylinder. *OpenFOAM® Journal*, 2:13–30, 2022.

[14] Hrvoje Jasak and Zeljko Tukovic. Automatic mesh motion for the unstructured finite volume method. *Transactions of FAMENA*, 30(2):1–20, 2006.

[15] Joris Degroote, Klaus-Jürgen Bathe, and Jan Vierendeels. Performance of a new partitioned procedure versus a monolithic procedure in fluid–structure interaction. *Computers & Structures*, 87(11-12):793–801, 2009.

[16] Nicolas Delaissé, Toon Demeester, Dieter Fauconnier, and Joris Degroote. Comparison of different quasi-newton techniques for coupling of black box solvers. In *14th World Congress on Computational Mechanics/8th European Congress on Computational Methods in Applied Sciences and Engineering*, 2021.

[17] C-K Kang, Hikaru Aono, Carlos ES Cesnik, and Wei Shyy. Effects of flexibility on the aerodynamic performance of flapping wings. *Journal of Fluid Mechanics*, 689:32–74, 2011.

[18] George Haller. Lagrangian coherent structures. *Annual Review of Fluid Mechanics*, 47:137–162, 2015.

[19] Gregory C Lewin and Hossein Haj-Hariri. Modelling thrust generation of a two-dimensional heaving airfoil in a viscous flow. *Journal of Fluid Mechanics*, 492:339–362, 2003.